THE EVOLUTION OF THE STAR FORMATION RATE OF GALAXIES AT $0.0 \leq Z \leq 1.2$

Wiphu Rujopakarn[1], Daniel J. Eisenstein[1], George H. Rieke[1], Casey Papovich[2], Richard J. Cool[3,11], John Moustakas[4], Buell T. Jannuzi[5], Christopher S. Kochanek[6], Marcia J. Rieke[1], Arjun Dey[5], Peter Eisenhardt[7], Steve S. Murray[8], Michael J. I. Brown[9], Emeric Le Floc'h[10]

ABSTRACT

We present the 24 μm rest-frame luminosity function (LF) of star-forming galaxies in the redshift range $0.0 \leq z \leq 0.6$ constructed from 4047 spectroscopic redshifts from the AGN and Galaxy Evolution Survey of 24 μm-selected sources in the Boötes field of the NOAO Deep Wide-Field Survey. This sample provides the best available combination of large area (9 deg^2), depth, and statistically complete spectroscopic observations, allowing us to probe the evolution of the 24 μm LF of galaxies at low and intermediate redshifts while minimizing the effects of cosmic variance. In order to use the observed 24 μm luminosity as a tracer for star formation, active galactic nuclei (AGNs) that could contribute significantly at 24 μm are identified and excluded from our star-forming galaxy sample based on their mid-IR spectral energy distributions or the detection of X-ray emission. Optical emission line diagnostics are considered for AGN identification, but we find that 24 μm emission from optically-selected AGN is usually from star-forming activity and therefore should not be excluded. The evolution of the 24 μm LF of star-forming galaxies for redshifts of $z \leq 0.65$ is consistent with a pure luminosity evolution where the characteristic 24 μm luminosity evolves as $(1 + z)^{3.8 \pm 0.3}$. We extend our evolutionary study to encompass $0.0 \leq z \leq 1.2$ by combining our data with that of the Far-Infrared Deep Extragalactic Legacy Survey. Over this entire redshift range the evolution of the characteristic 24 μm luminosity is described by a slightly shallower power law of $(1 + z)^{3.4 \pm 0.2}$. We find a local star formation rate density of $(1.09 \pm 0.21) \times 10^{-2}$ $M_\odot \mathrm{yr}^{-1} \mathrm{Mpc}^{-3}$, and that it evolves as $(1 + z)^{3.5 \pm 0.2}$ over $0.0 \leq z \leq 1.2$. These estimates are in good agreement with the rates using optical and UV fluxes corrected for the effects of intrinsic extinction in the observed sources. This agreement confirms that star formation at $z \lesssim 1.2$ is robustly traced by 24 μm observations and that it largely occurs in obscured regions of galaxies.

Subject headings: cosmology: observations — galaxies: evolution — galaxies: high-redshift — infrared: galaxies

1. INTRODUCTION

We have learned in the past 15 years that the star formation rate (SFR) of the universe peaked at a redshift of $z \geq 1$ and then rapidly declined by an order of magnitude to the present day (e.g., Lilly et al. 1996; Madau et al. 1996; Chary & Elbaz 2001; Hopkins 2004; Le Floc'h et al. 2005; Pérez-González et al. 2005; Hopkins & Beacom 2006) . The exact cause of the decline of the SFR remains unknown. However, since the period from $z \sim 0.6$ to the present encompasses nearly half of cosmic time coinciding with the SFR decline, this redshift range is a key regime for constraining the mechanisms that may be responsible.

The evolution of the SFR has been measured extensively at mid-IR (MIR; $8-30$ μm), far-IR (FIR), ultraviolet (UV), and optical wavelengths. Among these wavelengths, MIR and UV are ideal tracers for dust-obscured and unobscured galaxies, respectively. The MIR emission of galaxies originates from the reprocessed UV radiation of dust-embedded, highly obscured star-forming regions, and hence is sensitive to radiation from star formation that can not be seen directly at optical wavelengths (e.g., Kennicutt 1998; Buat et al. 1999). The stellar UV radiation field is largely created by hot OB stars ($M_* > 10$ $M_\odot$), which have very short lifetimes (< 20 Myr) and hence trace current star formation. The dust obscuration is generally substantial for star formation in galaxies at and above the characteristic luminosity L_* (Schmitt et al. 2006; Buat et al. 2007). Such galaxies comprise the majority of galaxies studied beyond the low redshift volume, so the MIR offers a relatively complete probe of SFR at intermediate and high redshifts. Among the IR wavelengths, the 24 μm-band is particularly suitable to study SFR evolution because it avoids most of the strong emission features from the stochastically heated

[1] Steward Observatory, The University of Arizona, Tucson, AZ 85721; wiphu@as.arizona.edu
[2] Department of Physics and Astronomy, Texas A&M University, College Station, TX 77843-4242.
[3] Department of Astrophysical Sciences, 4 Ivy Lane, Peyton Hall, Princeton University, Princeton, NJ 08544
[4] Center for Astrophysics and Space Sciences, University of California, San Diego, 9500 Gilman Drive, La Jolla, CA, 92093
[5] National Optical Astronomy Observatory, Tucson, AZ 85726.
[6] Department of Astronomy and the Center for Cosmology and Astroparticle Physics, The Ohio State University, 140 W. 18th Ave., Columbus, OH 43210.
[7] Jet Propulsion Laboratory, Mail Stop 169-506, California Institute of Technology, Pasadena, CA 91109.
[8] Harvard/Smithsonian Center for Astrophysics, Mail Stop 67, 60 Garden Street, Cambridge, MA 02138.
[9] School of Physics, Monash University, Clayton, Victoria 3800, Australia.
[10] Institute for Astronomy, University of Hawaii, Honolulu, HI 96822.
[11] *Hubble* Fellow

aromatic hydrocarbons (hereafter PAH) at wavelengths $3.3 < \lambda < 13\ \mu m$ for redshifts $z \lesssim 0.5$ while still avoiding the contamination from the Galactic IR cirrus at longer wavelengths (Shupe et al. 1998).

Measurements of IR number counts and luminosity functions (LFs) of galaxies demonstrate the rapid evolution of the SFR. Early IR studies utilized the *IRAS* Bright Galaxy Sample (Soifer et al. 1989) and the *IRAS* calibration field (Hacking & Houck 1987) and focused on accounting for the cosmic infrared background (CIB; Elbaz et al. 1999) with discreet MIR sources (Hacking et al. 1987; Saunders et al. 1990; Soifer & Neugebauer 1991). Studies of galaxy number counts with *ISO* and *Spitzer* have shown that IR galaxies evolve very strongly (Elbaz et al. 1999; Franceschini et al. 2001; Dole et al. 2004; Marleau et al. 2004; Papovich et al. 2004). As redshifts of IR samples became available, the LF could be constructed in the nearby volume (Rieke & Lebofsky 1986; Saunders et al. 1990; Yahil et al. 1991; Rowan-Robinson et al. 1997; Shupe et al. 1998) and subsequently extended to intermediate and high redshifts ($z > 3$) with large samples of photometric redshifts (Pozzi et al. 2004; Le Floc'h et al. 2005; Pérez-González et al. 2005; Caputi et al. 2007; Marleau et al. 2007) to study the SFR evolution over cosmic time. However, most of these studies were either in the local regime ($z < 0.1$) or at intermediate to high redshifts ($z > 0.5$). The redshift range $0.1 < z < 0.6$ includes more than 4 Gyr of galaxy evolution and needs to be characterized in detail to understand this process.

Observations of galaxy evolution at low and intermediate redshifts face two challenges. First, a large area, deep survey is required to access a large volume at lower redshifts, which is critical to minimize cosmic variance. For example, a deep survey at redshift $z \sim 0.5$ would need five times the solid angle coverage of one at $z \sim 1$ to probe a comparable comoving volume. Second, while photo-z's are generally adequate for distance determination at high redshift, accurate spectroscopic redshifts are critical at low and intermediate redshifts. To illustrate this issue, consider typical photometric redshift uncertainties of $\Delta z/(1 + z) = 0.05$. The corresponding fractional uncertainty in z would be a tolerable 10% at $z \sim 1$, while at $z \sim 0.25$ and below, the fractional uncertainty would exceed 25%. Also, photometric redshifts are only accurate for galaxies whose spectral energy distributions (SEDs) are well matched by either SED templates or, in the case of empirical photometric redshifts, galaxies in a spectroscopic training set. This may not be the case for heavily obscured galaxies such as luminous IR galaxies (LIRGs). In addition, the accuracy of some photometric redshift samples in the literature has not been verified with spectroscopy, and unknown systematic errors may be present.

In this work we construct the rest-frame 24 μm LFs of star-forming galaxies, measure their evolution, and estimate the SFR for $0.0 \leq z \leq 0.6$ from the LF. In addition to constraining the LF and SFR evolution accurately at low and intermediate redshifts, we combine our results with those from the Far-IR Deep Extragalactic Legacy Survey (FIDEL, Magnelli et al. 2009) to extend the constraints to $z \sim 1.2$. We organize this paper as follows. In Section 2 we discuss our *Spitzer* 24 μm sample, the spectroscopic redshifts from AGN and Galaxies Evolution Survey (AGES), the optical catalog from NDWFS, and address their completeness. In Section 3 we describe the construction of the LF, starting with the derivations of galaxy luminosities (Section 3.1), identification and exclusion of AGN from star-forming galaxies (Section 3.2), estimators for the LF (Section 3.3), parameterization of the evolution of the LF with redshift (Section 3.5), and the estimation of the SFR from the LF (Section 3.6). We then present the results in Section 4 for the local LF (LLF; Section 4.1), the LF evolution at low and intermediate redshifts (Section 4.2), the LF evolution constraint out to $z \sim 1.2$ (Section 4.3), as well as the SFR evolution of star-forming galaxies (Section 4.4). We summarize our results in Section 5. We assume a ΛCDM cosmology with $\Omega_m = 0.3$, $\Omega_\Lambda = 0.7$, and $H_0 = 70$ km s^{-1}Mpc^{-1} throughout this paper.

2. THE DATA

We construct the 24 μm LF of galaxies in the 9 sq. degree Boötes field of the NOAO Deep Wide-Field Survey (NDWFS Data Release 3; $\alpha = 14^h32^m$, $\delta = +34°16'$, J2000.0; Jannuzi & Dey 1999). The Boötes field has optical imaging reaching the 5-σ flux limit of 26.6, 26.0, 26.0, and 21.4 in B_W, R, I, and K (Vega magnitudes), respectively. Details about the NDWFS can be found in Jannuzi & Dey (1999) and at the survey's Web site[1].

In addition to the deep optical imaging, the Boötes field has extensive panchromatic coverage from other surveys, including an X-ray survey with the *Chandra* Space Telescope (XBoötes; Murray et al. 2005) comprising of 5 ks ACIS-I exposures, near-UV deep 30 ks imaging from *GALEX* (Martin et al. 2003), the IRAC Shallow Survey in the 3.6, 4.5, 5.8, and 8.0 μm bands reaching magnitudes of 19.1, 18.3, 15.9, and 15.2 mag (Vega mag), respectively, (Eisenhardt et al. 2004), the deeper *Spitzer* Deep, Wide-Field Survey (SDWFS, Ashby et al. 2009), and MIPS MIR photometry at 24 μm down to 0.27 mJy (Papovich et al. 2004; Houck et al. 2005). These imaging data are complemented by the set of optical spectroscopic redshifts from the AGN and Galaxy Evolution Survey (AGES; Kochanek et al., in prep.), which is a statistically complete redshift survey of the field at low and intermediate redshifts ($0 \leq z \leq 0.8$) (C. S. Kochanek et al., in preparation).

2.1. *Spitzer 24 μm-Observations, Reduction, and the Final Catalogue*

The 24 μm photometry in the Boötes field was obtained by the *Spitzer Space Telescope* wide-area survey with the Multiband Imaging Photometer for *Spitzer* (MIPS; Rieke et al. 2004) and processed with the MIPS GTO Data Analysis Tool (DAT; Gordon et al. 2005). The mean exposure time per pixel across the Boötes field is 87 s. The pixel size of the final mosaic is 1''.25 with a FWHM of 5''.7.

Source extraction from the final 24 μm mosaic was done using the techniques described in Papovich et al. (2004). Briefly, we weight the image by the typical integration time of each region to obtain uniform noise across the mosaicked image. We filtered the image with a Gaussian kernel similar to our 24 μm point-spread function

[1] http://www.noao.edu/noao/noaodeep

(PSF) to remove artifacts and optimize point-source detection and then used DAOPHOT (Stetson 1987) to detect sources. The actual photometric measurement was carried out by fitting empirical PSF constructed from bright sources in the image. Based on Monte Carlo simulations by Papovich et al. (2004) the 80% completeness flux threshold is $F_\nu(24\ \mu m) = 0.27$ mJy, and there are 8,572 objects in our sample above this flux level.

The MIPS survey of the Boötes field combines considerable depth with a large contiguous area of 32,457 arcmin^2 (9.0 deg^2). While many other fields have been surveyed to deeper $F_\nu(24\ \mu m)$, such as the GOODS, ELAIS and CDF-S fields (Pozzi et al. 2004; Le Floc'h et al. 2005; Chary 2007; Elbaz et al. 2007) with 80% completeness flux of 25 μJy, 61 μJy and 83 μJy, respectively, they also cover significantly smaller area (0.011 deg^2, 0.036 deg^2, and 0.407 deg^2, respectively), and therefore encompass significantly smaller volumes at low and intermediate redshifts. The Cosmic Evolution Survey (COSMOS, Scoville et al. 2007) has a large sample of spectroscopic redshifts (Lilly et al. 2007) and deep, $\sim$80 μJy, 24 μm imaging (LeFloc'h et al. 2009). The 2 deg^2 area of the COSMOS field is one of the best combinations of large area and depth at higher redshifts; however, a larger angular coverage is still required to suppress the effects of cosmic variances at low and intermediate redshifts. The available large-area MIR surveys, such as the *Spitzer* Wide-area Infrared Extragalactic Survey (SWIRE) and the European Large Area *ISO* Survey (ELAIS, 15 μm), currently lack thorough spectroscopic redshifts.

2.2. *Optical Spectroscopy Target Selection, Observation, and the Final Catalogue*

The Boötes field was observed spectroscopically by the AGES during 2004-2006 using the Hectospec spectrograph in a survey region of 7.9 deg^2 (C. S. Kochanek et al., in preparation). Hectospec is a fiber-fed spectrograph with 300 robotically assigned fibers covering a 1-degree diameter field of view at the $f/5$ focus of the 6.5-meter MMT Observatory (Fabricant et al. 2005). AGES produced $\sim$20,000 redshifts, of which $\sim$16,500 and $\sim$3,500 are galaxies and quasars, respectively, with redshift uncertainties less than $\sigma_z \sim 100$ km s^{-1} (as in the similar survey by Papovich et al. (2006)) and a median galaxy redshift of $z = 0.26$ (C. S. Kochanek et al., in preparation).

Targets for spectroscopy were principally selected on the basis of their optical magnitudes. AGES targeted galaxies to $I_C < 20$, where I_C is the Kron-like magnitude (in Vega units) in the Kron-Cousins I-band of the ND-WFS (SExtractor's `MAG_AUTO`; Bertin & Arnouts 1996). For galaxies brighter than $I_C = 18.5$, there was full sampling. For fainter galaxies with $18.5 < I_C < 20$, AGES used random sparse sampling of 1 in 5 galaxies, with rates that depended on a variety of other factors, so as to put emphasis on more unusual objects. Additional targets were added to the spectroscopic sample if they were brighter than certain flux limits in the X-ray, infrared, other optical bands, and radio. For example, all galaxies with $F_\nu(24\ \mu m)$ above 0.5 mJy were targeted, as well as 30% of those down to 0.3 mJy. For each object, the a priori sampling rate is known and so the object

can be exactly weighted to form an unbiased sample of $I_C < 20$ galaxies. AGES observed the Boötes field with 15 complete tilings, so the completeness for the target galaxies is very high. Our final sample has 4.3% incompleteness due to difficulties in assigning fibers to targets and 2.1% incompleteness due to failing to get a successful redshift from an assigned fiber. We also estimate that the parent photometry catalog is missing 4% of the objects in the range $15 < I_C < 20$, half of which is due to interference by nearby bright stars, the rest likely due to blending and corruption of the parent photometry. We model these mild incompletenesses, including factors for areal target density and surface brightness, and correct the final weights of objects in the redshift catalog (R. J. Cool et al., in prep.). As the total incompleteness correction is only 10%, it is very likely that the systematic error in the correction is far less than the Poisson and cosmic variance in our results.

Each Hectospec fiber is 1″5 in diameter and produces a spectrum covering the wavelength range of 3500 Å $\leq \lambda \leq 9200$ Å with 6 Å FWHM resolution ($R \sim 1,000$). Typical signal-to-noise ratios of the AGES spectra are $2 - 14$ per pixel with a median of 5 per pixel. We fit redshifts to AGES with two automated pipelines, one based on the SDSS template-fitting code, the other on cross-correlations. The pipelines make use of spectral features across the spectral range (absorption lines, emission lines, and spectral breaks due to metal-line absorptions) and hence result in accurate redshifts regardless of whether a particular spectral line is compromised (e.g. by overlap with sky lines). The two pipelines gave broadly consistent results. In addition, we visually examined every fit. Any objects with visually questionable results were tagged for reobservation, since AGES covered the full field in six sequential passes. The result is a spectroscopic catalog with high completeness and high reliability. The spectroscopic success rate, after fiber assignment, is 98%, and we expect the redshift error rate on claimed successes to be well below 1%. Any systematic biases due to errors in the completeness corrections or the redshift catalog are likely to be considerably smaller than the statistical errors of our LF.

In the redshift range of interest, $0.05 \leq z \leq 0.65$, we have redshifts for 4,047 objects with $F_\nu(24\ \mu m)$ above the 80% completeness limit of 0.27 mJy.

3. INFRARED LUMINOSITY FUNCTION

Here we describe the construction of the 24 μm LF. We start by estimating the 24 μm and optical (I-band) rest-frame luminosities, then identify and exclude AGN in our sample, and finally construct the LF using the classical $1/V_{max}$ (Schmidt 1968; Huchra & Sargent 1973) and the maximum likelihood estimator (MLE; e.g., Sandage et al. 1979; Marshall et al. 1983; Yahil et al. 1991). Later in this section, we describe the parameterization of LF evolution, which will be used to study the evolution of the SFR.

3.1. *24 μm and I-band Luminosity Estimation*

In addition to the obvious need for 24 μm luminosities, $L(24\ \mu m)$, to construct the LF, we have to compute the I-band luminosity for each galaxy. AGES spectroscopy was targeted based on an I-band, flux-limited

parent catalog. Hence, an object can only be included in the final LF sample if it is detected above the flux limits at both 24 μm and I-band. Therefore, the luminosities in both bands are needed for estimating the maximum redshift, z_{max}, that an object would still be detected in both bands to the construct the $1/V_{max}$ LF. $L(24~\mu\text{m})$ is estimated by the formalism given by Rieke et al. (2009). For the I-band, we derive the I-band k-correction using the `kcorrect` code (Blanton & Roweis 2007) and then use the k-correction to estimate the I-band luminosity.

The I-band k-corrections were derived using optical photometry from NDWFS and redshifts from AGES. A fraction of our I-band objects are affected by scattered light from bright stars. Specifically, some of the NDWFS I-band Kron-like magnitudes (SExtractor's `MAG_AUTO`), I_C, are overly bright due to contamination from low-surface-brightness halos of nearby bright stars. This problem can be corrected by synthesizing a new I-band magnitude, I_R, by adding a Kron-like magnitude in R-band, R_C, to the $I - R$ color from 6″ apertures ($I_R = R_C + I_{6''} - R_{6''}$). This synthesized I_R is less sensitive to the I-band halo than I_C. Then we compare I_R to I_C to compute a new I-band magnitude, I_{total}, that uses the fainter magnitude if the two differ significantly; otherwise we average them (R. J. Cool et al., in preparation). The I_{total} computation is done in a way that the continuity of the magnitudes is preserved. In the cases that require averaging I_R and I_C, the differences are on the order of a tenth of a magnitude and hence averaging a logarithm does not introduce a significant bias. We note that the aperture correction is insensitive to the choice of estimation procedure and that the final LFs are little affected by this correction, ultimately because the I-band generally has deeper photometry than at 24 μm and hence most of the values of z_{max} will be limited by the 24 μm photometry. Apart from the I_{total} for I-band photometry, we use the 4″-diameter aperture magnitude from NDWFS for the B_W and R bands to perform k-correction estimation. We adopt the following corrections to convert the Vega zero points to AB: +0.02 mag, +0.19 mag, and +0.44 mag in B_W, R, and I, respectively. The Galactic extinction for our field is $A_I = 0.02$ mag (Schlegel et al. 1998).

The estimation of $L(24~\mu\text{m})$ requires an assumption for the spectral energy distribution (SED) of a galaxy in the IR regime, which has been modeled by many authors (e.g., Dale et al. 2001; Chary & Elbaz 2001; Dale & Helou 2002; Lagache et al. 2003, 2004; Smith et al. 2007; Dale et al. 2007). More recently, Rieke et al. (2009) constructed a library of SEDs by combining stellar photospheric spectra from $0.4-5~\mu$m with *Spitzer* IRS spectra from $5-30~\mu$m and a modified blackbody spectrum at longer wavelengths for 11 representative local Luminous IR galaxies (LIRGs; $10^{11}L_\odot < L(\text{TIR}) < 10^{12}L_\odot$) and ultraluminous IR galaxies (ULIRGs; $L(\text{TIR}) > 10^{12}L_\odot$). Higher $L(\text{TIR})$ galaxies contain more intense star-forming activity and hence a larger fraction of warm dust, leading to changes in the SED with IR luminosity.

Normally, the derivation of SFR from MIR photometry involves selecting the SED that best matches the object's luminosity given its MIR flux and redshift, integrating this SED to obtain $L(\text{TIR})$, and then using a SFR

metric to calculate the SFR. However, this procedure implies fitting a SED with only one data point, 24 μm in our case, because the number of objects that are detected in multiple MIPS bands is very limited, which could lead to significant uncertainties. Rieke et al. (2009) circumvented this problem by first assigning a SFR to each SED, which has a unique $L(\text{TIR})$. They then derive a flux in the relevant band pass (24 μm) over a range of redshifts.

Given that $L(\text{TIR})/L(24~\mu\text{m}) \sim 10$ (e.g., Rieke et al. 2009), our sample with galaxies mainly in the 24 μm luminosity range $10^{8.5} < L(24~\mu\text{m}) < 10^{10.5}$ (Figure 1), is dominated by normal star-forming galaxies ($L(\text{TIR}) < 10^{11}L_\odot$). Figure 1 also illustrates that LIRGs only start contributing significantly to the MIR luminosity density at redshifts greater than $z = 0.2$. Although ULIRGs start to appear in our sample at $z \sim 0.4$, we will demonstrate in Section 3.2.4 that they are mostly AGN and we will exclude them from our sample of star-forming galaxies.

3.2. Separating Star-Forming Galaxies and AGN Hosts

To quantify the 24 μm emission due to star formation, we need to minimize the contribution of AGN. There are several methods to identify AGN in a galaxy sample. Optical emission line diagnostics such as the BPT method (Baldwin et al. 1981) are commonly used when optical spectra are available. MIR power-law characteristics of AGN (e.g., Alonso-Herrero et al. 2006; Donley et al. 2007) and MIR color criteria (e.g., Lacy et al. 2004; Stern et al. 2005) can be used if multi-band MIR photometry is available. X-ray emission is also a direct indicator of AGN activity. Since the Boötes field has multiwavelength coverage that permits using all these, we investigate all of them in this section.

3.2.1. Optical Emission Line AGN Diagnostics

In addition to identifying the broad-line AGN (type 1), our spectroscopic survey allows us to identify narrow-line AGN (type 2) in the sample using the BPT diagram. We require that all four relevant lines (Hα, Hβ, [OIII], and [NII]) are detected at S/N > 3. Thus, the BPT method can only be used for redshift of $z < 0.35$ because at higher redshifts the Hα emission line shifts beyond the red limit of the spectral range covered by Hectospec. We identify AGN on the BPT diagram (Figure 2, left) as objects with line ratios above the theoretical limit (hereafter the Kewley line; Kewley et al. 2001, 2006) of ratios that star-forming regions could produce. The Kewley line was estimated by considering all possible combinations of star-forming galaxy spectra based on the `Starburst99` (Leitherer et al. 1999) models. Objects above the Kewley line will be referred to hereafter as *optically selected AGN*. We identified 421 optically selected AGN at $0.0 \leq z \leq 0.35$, 46% of which (192/421) have $F_\nu(24~\mu\text{m}) > 0.27$ mJy.

However, we need to determine whether the 24 μm emission from optically selected AGN is actually dominated by the AGN. Our $1''.5$ diameter spectroscopic fiber would cover a distance of 6 kpc at the median redshift of the AGES sample ($z = 0.26$) and the fiber would be placed at the center of the target galaxy. Thus our BPT classification would be sensitive to the nuclear flux from
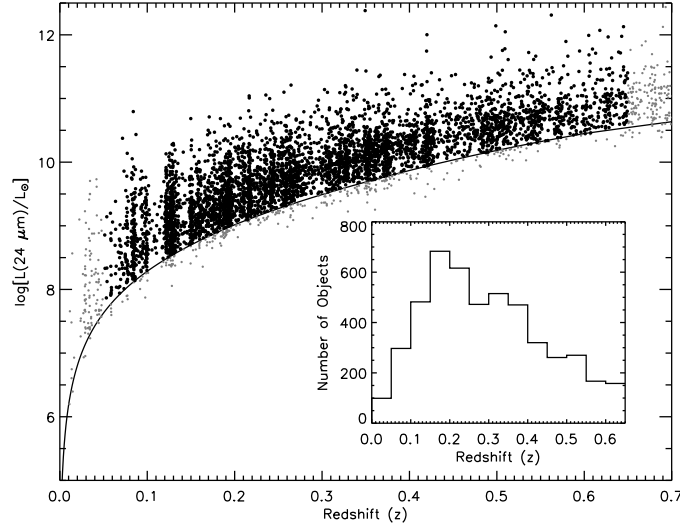
Figure 1. Redshift distribution of the rest-frame 24 μm luminosity for our sample. The gray dots show all 24 μm galaxies with spectroscopic redshifts from AGES. The black dots are those above the 24 μm completeness flux limit (0.27 mJy) at $0.05 \leq z \leq 0.65$ that we use to construct the LF. The line indicates the $L(24 \mu m)$ corresponding to this completeness flux threshold as a function of redshift. Inset: the redshift distribution of the AGES objects detected at 24 μm.
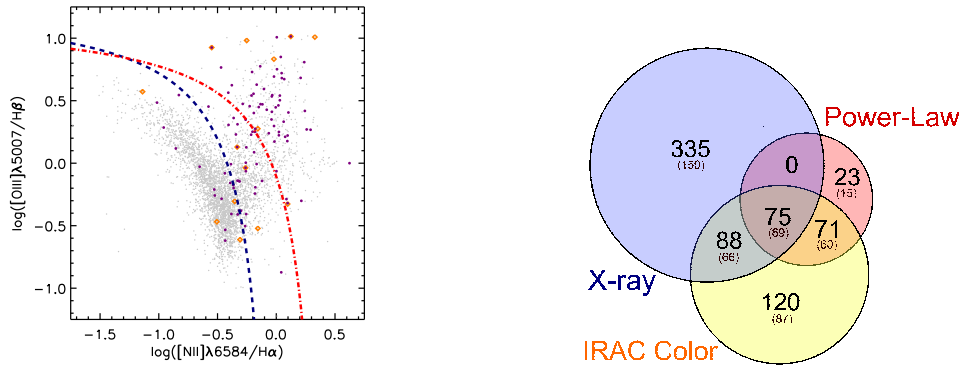

Figure 2. Left: optical selection of AGN using the BPT diagram. Orange diamonds and magenta dots are power-law and X-ray selected AGNs, respectively. The Kewley and Kauffmann lines are shown by red dot-dashed line and blue dashed line, respectively (Kewley et al. 2001; Kauffmann et al. 2003). Many power-law and X-ray selected AGN are identified as star-forming galaxies by the BPT diagram. Note that a large fraction of power-law and X-ray selected AGN are not shown here because they do not have sufficiently strong emission lines to apply the BPT diagnostic and most of them are at $z > 0.35$ where Hα line redshifts out of the Hectospec spectrum. Right: the Venn diagram for 712 AGNs at $0.0 \leq z \leq 0.65$ to illustrate the overlapping of AGN identified by X-ray detections, power-law fitting, and the (Stern et al. 2005) color criteria. The numbers in each area and the numbers in parentheses are the total numbers of objects and the numbers of objects detected at 24 μm, respectively. 288 of 712 AGNs in this Venn diagram are detected at 24 μm, pass all quality cuts, and are in the main galaxy sample. They are excluded from the sample to obtain the star-forming galaxy sample that can be accurately used as a tracer of star formation.

the AGN but could miss the emission lines contributions from star-forming regions outside the fiber. In the case that star formation dominates the global optical emission but an AGN dominates the emission within the fiber, the global 24 μm flux could in fact be dominated by the emission from star-forming activity and excluding such objects would lead to an underestimation of the star formation rate.

We therefore investigate the origin of mid-IR emissions from the optically selected AGN by studying the IRAC colors of these AGN. Using IRAC photometry from the IRAC Shallow Survey (6″ aperture, Section 2), we study the [3.6 μm] − [4.5 μm] versus [5.8 μm] − [8.0 μm] color-color diagram (hereafter, [3.6]−[4.5] and [5.8]−[8.0], respectively) for optically selected AGN (Figure 3, left). The color-color diagram can be used to identify MIR aromatic emission characteristic of star formation activity (Smith et al. 2007; Shi et al. 2007), because the

strongest aromatic features at 6.2, 7.7, and 8.6 μm fall into the 8.0 μm band (channel 4; $\simeq 6.2 - 10 \mu$m) at redshifts $0.0 \leq z \leq 0.5$. This behavior results in a redder [5.8]−[8.0] color for objects with MIR aromatic emission, which also implies that the MIR emission of these objects is dominated by star formation. The empirical color boundary that separates the aromatic and non-aromatic region is [5.8]−[8.0] $\simeq 1$ (Brand et al. 2009). We found optically selected AGN distributed across the full range of [5.8]−[8.0] color. However, if we further separate optically selected AGN into those detected at 24 μm and those that are not, they split into two locales. Optically selected AGN without 24 μm detection are relatively blue in [5.8]−[8.0] color while more than 70% of those with 24 μm detection congregate in the aromatic locus. The bluer MIR locus of optically selected AGN without 24 μm detection is consistent with the Rayleigh-Jeans tail of an old stellar population's photospheric emission that peaks
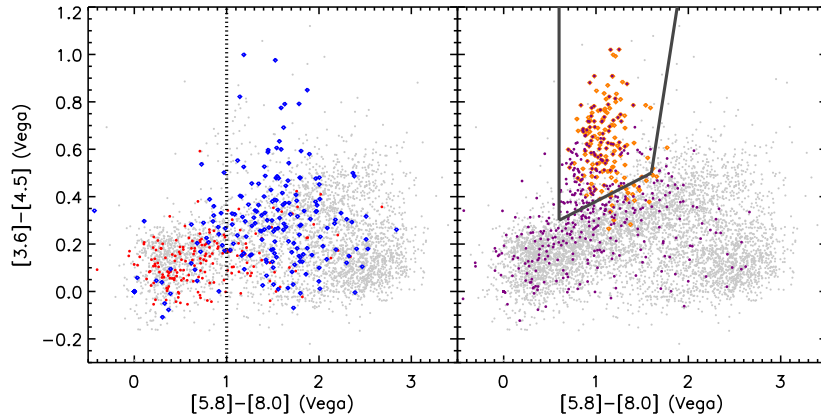
Figure 3. Mid-IR properties of AGNs in our sample. Left: the [3.6]−[4.5] vs. [5.8]−[8.0] color-color diagram separates objects with and without aromatic emissions at an empirical boundary of [5.8]−[8.0] ∼ 1 (vertical line, Brand et al. 2009), with aromatic-emitting objects on the redder [5.8]−[8.0] side. Blue and red dots represent optically selected AGN with and without 24 μm detection, respectively. Right: the same diagram showing the Stern et al. (2005) AGN selection criteria (trapezoidal box), power-law selected AGN (orange diamonds), and X-ray selected AGN (magenta dots). A majority of optically selected AGN that emit strongly at 24 μm are aromatic-emitting objects and their MIR emission is likely dominated by star-forming activity. On the other hand, a majority of X-ray selected AGN share the same locus as power-law selected AGN, indicating that their AGN component could contribute significantly at 24 μm.

at 1.6 μm. This suggests the source of 24 μm emission in an optically selected AGN is likely to be star-forming activity, not the AGN.

3.2.2. X-ray Detections

We have also searched for AGN detected in the 5 ks X-ray survey of the Boötes field (XBoötes; Murray et al. 2005). We define an *X-ray selected AGN* as any source with two or more X-ray counts and a > 25% probability based on the Bayesian matching method described by Brand et al. (2006). Since XBoötes is designed to have a large contiguous area and a shallow flux limit, X-ray identification based on the survey will only identify the strongest AGN. The X-ray luminosities of these sources are typically brighter than 10^{42} ergs^{-1} (Hickox et al. 2009) and hence they are unlikely to be dominated by star-forming activity. Although it is not possible to infer directly the AGN contribution to the 24 μm flux from the strength of the X-ray emission, strong AGN are known to emit significantly in the MIR (e.g., Barmby et al. 2006). We found 498 X-ray selected AGN at $0.0 \leq z \leq 0.65$ and 175 of them are at the redshift range where we construct the LF ($0.05 < z < 0.65$), are in the main galaxy sample, and are detected at 24 μm.

3.2.3. MIR AGN Diagnostics

AGN with significant MIR emission can be identified most directly by applying MIR selection methods. MIR photometry can be used to identify luminous AGN due to their characteristic power-law SED rising from the optical wavelengths to the IR. This power-law SED is due to the combination of thermal emission of warm and hot dust components and non-thermal emission of the nuclear region (Neugebauer et al. 1979; Elvis et al. 1994; Rieke & Lebofsky 1981). AGN can be identified by fitting a power law, $F_\nu = \nu^\alpha$, to all four bands of IRAC photometry covering 3.6 - 8 μm (Eisenhardt et al. 2004) with χ^2 minimization. We require an object to be detected in all four bands at above 5-σ for power-law fitting. *Power-law selected AGN* are defined as

galaxies exhibiting power-laws with α ranging from −0.5 to −2.0 (Ivezić et al. 2002; Alonso-Herrero et al. 2006; Donley et al. 2007). The power-law method identified 169 AGN. Among these AGN, 144 are detected at 24 μm (85%), which is the highest fraction among the AGN classification methods. This suggests that the 24 μm emission of power-law selected AGN is an extension of their power-law AGN SED to longer wavelengths rather than from the warm dust characteristic of star-forming galaxies. Therefore the power-law selection of AGN provides a good basis to exclude AGN from our 24 μm star-forming galaxy sample. However, the signal-to-noise requirement on the IRAC photometry for power-law fitting affects the completeness of power-law AGN selection. Among these 169 AGN, 73 are at $0.05 < z < 0.65$ and pass all targeting and quality cuts, and are detected at 24 μm.

Another manifestation of power-law SED of AGN is their locus on MIR color-color diagrams (Section 3.2.1). Again, we consider the [3.6]−[4.5] vs. [5.8]−[8.0] color-color diagram. AGN (mostly type 1) exhibit power-law SEDs and this results in a distinct locus that is significantly redder in the [3.6]−[4.5] color than both early type and star-forming galaxies (see Figure 1 of Stern et al. 2005). The locus of early type galaxies, which also exhibit power-law SEDs but with $\alpha > −0.5$, would lie blueward in both color indices (lower-left locus on the diagram) because, as mentioned earlier, their SEDs in the NIR are dominated by the Rayleigh-Jeans tail of old stellar populations. Stern et al. (2005) empirically define the AGN locus on the color-color diagram (the "Stern wedge", Figure 3, right). AGN selected based on this color-color criteria (hereafter *IRAC color selected AGN*) are defined by galaxies with ([5.8] − [8.0]) > 0.6 and ([3.6]−[4.5]) > 0.2([5.8]−[8.0])+0.18 and ([3.6]−[4.5]) > 2.5([5.8] − [8.0]) − 3.5. We found 354 IRAC color selected AGN in the redshift range $0.0 \leq z \leq 0.65$, 80% (282/354) of which have 24 μm detections. A majority (86%, 146/169) of the power-law selected AGN are also selected by the Stern et al. (2005) criteria. The reverse is not the case: only 41% (146/354) of IRAC color
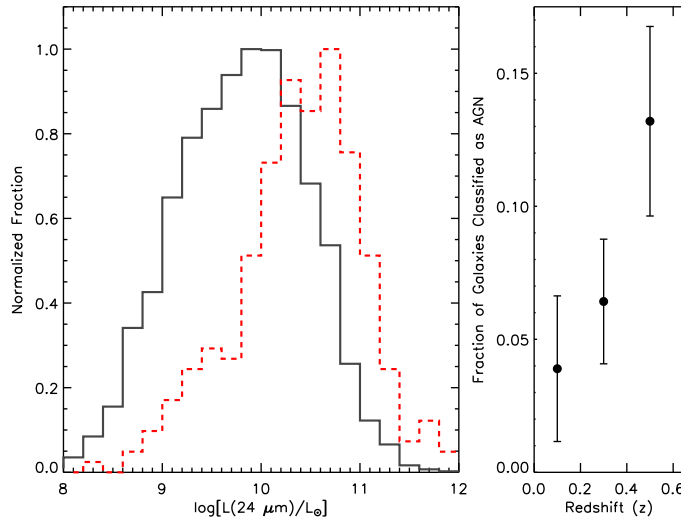
Figure 4. 24 μm luminosity distribution of the star-forming and AGN sub-samples at $0.05 \leq z \leq 0.65$. Left: the rest-frame $L(24 \mu m)$ distribution of 3,759 star-forming galaxies (solid histogram) and 288 AGNs (dashed histogram) identified by their characteristic power-law SED (based on power-law fitting and IRAC colors) and X-ray detections that pass all targeting and quality cuts. Right: the fraction of galaxies identified as AGN in our sample rises with redshift at $z \lesssim 0.6$. This is partly due to the fact that AGNs are intrinsically more luminous, as shown in the left panel. ULIRGs (galaxies with $L(IR) > 10^{12} \ L_\odot$ or $L(24 \mu m) > 1.5 \times 10^{11} \ L_\odot$) are dominated by galaxies exhibiting AGN activity that are excluded from our LFs of star-forming galaxies.

selected AGN exhibit identifiable power-law characteristics. However, Figure 3 (right) illustrates that there are a few galaxies in the power-law selected AGN locus but not identified as AGN by the MIR power-law fitting. These galaxies satisfy the Stern et al. (2005) criteria, which suggests that adopting the Stern et al. (2005) AGN selection criteria helps augment the completeness of power-law AGN selection in our case. Among these 354 IRAC color selected AGN, 159 are at $0.05 < z < 0.65$ and pass all targeting and quality cuts, and are detected at 24 μm.

As another test for MIR-emitting AGN, we used the behavior of the IRAC $[5.8] - [3.6]$ color. For $z \geq 0.2$, both bands should be on the Rayleigh-Jeans tail of the photospheric SED without substantial contamination by infrared excess emission from normal star formation (see, e.g., the Rieke et al. (2009) SED templates). However, the warm dust around an AGN should appear as an anomalously red color. Many of the objects identified in this way are still dominated by aromatic emission, as judged by their full set of IRAC colors. However, a small fraction (21 objects at $0.05 < z < 0.65$) may have IR excesses associated with AGN that are not identified by other methods. These 21 objects amount to only 7% of our AGN sub-sample. Without other independent AGN signatures we cannot determine whether the 24 micron emission of these galaxies is dominated by AGN. Our results are independent, within the errors, of whether we include or exclude these sources from our star-forming galaxy sample.

3.2.4. *Summary of Multiwavelength AGN Selection*

We found that optical line diagnostics (the BPT diagram) select AGN that frequently have 24 μm fluxes dominated by emission from star formation (Section 3.2.1) and therefore that these diagnostics should not be used as a basis to exclude AGN from the MIR

star-forming galaxy sample. Methods based on power-law characteristic of AGN (power-law SED selection (Donley et al. 2008) and color criteria, e.g. Stern et al. (2005)) yield AGN samples more relevant to our 24 μm study (Section 3.2.3). On the $[3.6]-[4.5]$ vs. $[5.8]-[8.0]$ color-color diagram, X-ray selected AGN occupy regions encompassing the locus of power-law selected AGN and extend toward the bluer $[5.8]-[8.0]$ and $[3.6]-[4.5]$ color regions (Cardamone et al. 2008; Gorjian et al. 2008), indicative of older stellar populations, suggesting that X-ray selection helps augment the completeness of AGN selection by the MIR selection methods. Therefore we combine MIR selection of AGN with X-ray selection to create a list of AGN to be excluded from our 24 μm LF study.

The Venn diagram (Figure 2, right) illustrate the significant overlapping of AGN selected by X-ray, Power-law fitting, and the Stern et al. (2005) criteria. At $0.0 \leq z \leq 0.65$, we find a total of 712 AGNs, 288 of which are detected at 24 μm, pass all targeting and quality cuts, and are in the redshift range $0.05 \leq z \leq 0.65$ where we use to construct LFs. Figure 4 illustrates the fraction of AGN as a function of 24 μm luminosity and redshift. Note that objects with $L(24 \mu m) > 10^{11} \ L_\odot$ are mostly AGN. Most of the trend in the AGN fraction with redshift seen in Figure 4) are a consequence of the increasing fraction of AGN at higher $L(24 \mu m)$. Higher redshift bins are dominated by higher luminosity galaxies because of the survey flux limit and hence will show higher AGN fractions.

Excluding these 288 AGNs from the 4,047 galaxies at $0.05 \leq z \leq 0.65$ that are detected at 24 μm, we obtain a sub-sample of 3,759 star-forming galaxies to construct the LFs.

3.3. *Methodology*

We estimate our LF at redshift $0.05 \leq z \leq 0.65$ using the $1/V_{max}$ formalism (Schmidt 1968; Huchra & Sargent 1973), and the local 24 μm LF (hereafter *local LF* or *LLF*) using the parametric maximum likelihood estimator (MLE; e.g., Sandage et al. 1979; Yahil et al. 1991; Marshall et al. 1983). The local LF is then evolved to fit the higher redshift $1/V_{max}$ LFs using a χ^2 minimization to determine the evolution of the LF as a function of redshift (Section 3.5).

The $1/V_{max}$ estimator is non-parametric in the sense that it does not assume a functional form for the LF. However, it is sensitive to density variations due to large scale structures. The large areal coverage of the ND-WFS helps to mitigate this problem. But at the lowest redshifts that we observed, even a 9 sq. deg field covers a sufficiently small volume to show significant cosmic variance. The most prominent example is a ~50% over-density near $z \simeq 0.15$ (see Figure 1).

We construct the $1/V_{max}$ LF by first computing a spectroscopic selection function that takes into account the parent catalog's incompleteness due to imaging and targeting issues. These issues include sparse sampling due to priority conflicts in Hectospec fiber assignment, incompleteness due to fiber allocation limits (such as the proximity limit), and redshift extraction failure (Section 2.2). The selection function is then applied to each galaxy as a weight, w_i, that corrects for incompleteness. The V_{max} in our analysis is taken to be the volume enclosed by the maximum redshift that allows an object to be included in both our I-band (spectroscopic targeting) and 24 μm samples. That is, we take the smaller of the redshift at which $F_\nu(24 \ \mu m)$ would drop below 0.27 mJy or the redshift at which the object will have $I_C > 20$ mag. We estimate the $1/V_{max}$ LF in four independent redshift bins ranging from redshift $z = 0.05$ to $z = 0.65$ with a bin width of 0.15. The lowest redshift region (e.g. $z < 0.05$) was excluded to avoid potentially unrealistic number densities due to the very small volume and number of galaxies and also to minimize the effect of photometric bias due to nearby, large galaxies that extend beyond our 24 μm PSF. This redshift cut excludes only 82 objects (2% of the sample). In each bin, we take V_{min} to be the volume enclosed by the z_{max} of the adjacent lower redshift bin.

The MLE method was used to determine the shape of the local 24 μm luminosity function (LLF). MLE requires no binning of data and is insensitive to density variations, which is ideal for the lowest redshift regime where large scale structures affect the $1/V_{max}$ LF the most. We parameterize the LF with the double-power law proposed by Yahil et al. (1991).

$$\Psi(> L) = C \left(\frac{L}{L_*} \right)^{-\alpha} \left(1 + \frac{L}{L_*} \right)^{-\beta}, \qquad (1)$$

which corresponds to the differential luminosity function

$$\Phi(L) = \left(\frac{\alpha}{L} + \frac{\beta}{L + L_*} \right) \Psi(> L). \qquad (2)$$

This functional form is commonly used to describe the MIR luminosity function (Shupe et al. 1998; Xu et al. 1998; Xu 2000; Sanders et al. 2003; Magnelli et al. 2009). The Xu (2000) template was also used by Le Floc'h et al.

(2005) to describe MIR LF evolution to $z \sim 1$. It should be noted that the turnover of the Schechter function (Schechter 1976) frequently used for optical LFs is too steep to fit the IR LF (Rieke & Lebofsky 1986; Yahil et al. 1991; Le Floc'h et al. 2005).

We determine the parameters by maximizing the likelihood function over the parameter space of the bright-end slope, α, the faint-end slope, β, and the characteristic luminosity, L_*, using the sample members in the redshift range of $0.05 \leq z \leq 0.25$. The normalization factor, C, has to be determined separately (since the factor cancels and does not appear in the likelihood function) by matching the integrated number density expected from MLE to that observed in the $1/V_{max}$ LF of the same sample. We constructed the LLF for both star-forming and all-galaxy samples.

For the purpose of constructing a local luminosity function, the redshift range $0.05 \leq z \leq 0.25$ cannot be considered purely local. Especially with a population with the strong luminosity evolution of IR galaxies, the L_* estimate from such a wide redshift range would inherently be brighter than the true local L_*. To illustrate this, if we assume that the luminosity of IR galaxies evolves as $(1 + z)^{3.3}$ and the median redshift of the sample used for the LLF is $z = 0.15$, we would expect a 60% luminosity increase from the actual $L_*(z = 0)$. There are a number of possible approaches to solve this problem. The first is to fit the luminosity evolution as a parameter in the MLE simultaneously while constraining the shape parameters. In practice such a fit would be difficult due to the additional free parameters and the degeneracy between luminosity and density evolution. One might need to fix some shape parameters (such as the faint-end slope) to achieve a plausible fit. The second approach would be to limit the redshift range of the sample to estimate the LLF. However, reducing the redshift bin size would compromise the constraints on the bright-end slope; we need to estimate the LLF using a sample selected to $z \leq 0.25$ to encompass enough volume to find rare, bright galaxies. Others have faced the same problem. The Shupe et al. (1998) and Xu (2000) LLFs contain few bright galaxies as far as $z \sim 0.2$. Although their median redshift is much closer to local, the luminosity evolution could result in a more luminous L_* than the true local value. Another way to limit the redshift range to the local volume would be to rely on an MIR sample from all-sky IR surveys with shallow limiting fluxes such that the sample is limited to very nearby galaxies. But since all-sky surveys lack complete spectroscopic redshift follow-up and usually have to compile redshifts from several catalogs, the spectroscopic selection function of the combined sample may not be well understood. Robustly constraining a true local L_* is important because the local L_* is often used to constrain the evolution of the LF at higher redshifts, such as in Le Floc'h et al. (2005), who used the Sanders et al. (2003) local L_* derived from the IRAS 60 μm-selected sample.

Our solution to this problem is to take advantage of the evolution information in our full sample, an option not available to studies limited to $z \lesssim 0.2$. The evolution constraint from the higher redshifts can be used to constrain the evolution and extrapolate L_* back to the true value at $z = 0.0$ (Section 3.5).

Table 1
Parameters of the Mid-IR Local Luminosity Function in Comparison with Other Works

Reference[a]	α	β	$L_*(24\ \mu\mathrm{m})$ $(10^9 \mathrm{L}_\odot)$	C $(10^{-3}\mathrm{Mpc}^{-3})$
All Galaxies	0.36 ± 0.04	2.17 ± 0.35	4.07 ± 0.67	1.2 ± 0.8
Star-Forming	0.37 ± 0.04	2.36 ± 0.41	4.27 ± 0.71	1.2 ± 0.8
Shupe et al. (1998)	0.437 ± 0.032	1.749 ± 0.067	4.47 ± 0.40	1.0 ± 0.6
Xu et al. (1998)	0.47 ± 0.13	2.20 ± 0.13	6.40 ± 2.25	0.9 ± 0.5
Sanders et al. (2003)	0.6 ± 0.1	2.2 ± 0.1	4.4	0.8^{b}

[a] Results from other studies are corrected for their bandpass differences to reflect estimates at 24 μm using the Rieke et al. (2009) SED library. Redshift ranges for each study are the following. This study: $0.05 \leq z \leq 0.25$, median redshift of 0.17 in both samples, with L* evolve back to $z = 0.0$ (for both all-galaxy and star-forming sample) simultaneously with the evolution fit (see Section 3.5); Shupe et al. (1998): $0.001 \leq z \leq 0.07$; Xu et al. (1998): $0.02 \leq z \leq 0.22$; Sanders et al. (2003): median and mean redshifts of 0.0082 and 0.0126, respectively.
[b] Sanders et al. (2003) do not report their normalization explicitly but a power-law break fit to their $1/V_{max}$ LLF (see their Table 6) suggests a value of 8×10^{-4} Mpc^{-3}.
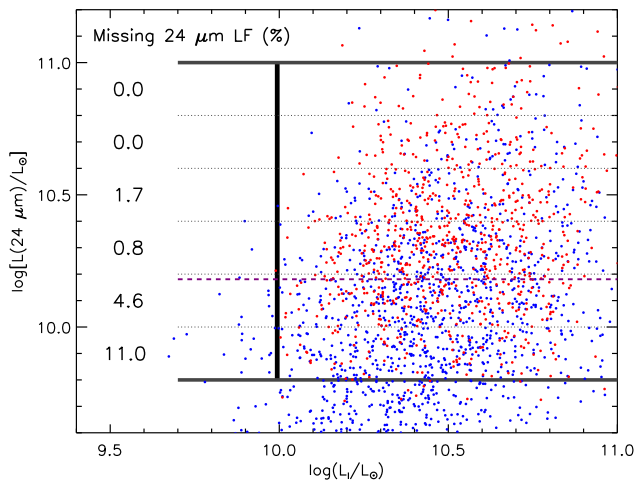

Figure 5. 24 μm and I-band bivariate luminosity functions (BLF) were constructed to quantify the effects of incompleteness at 24 μm of MIR-bright, optically-faint galaxies (the *bivariate selection bias*). The BLF construction to quantify the bivariate selection bias for the sub-sample at redshift $0.35 \leq z \leq 0.5$ is illustrated in this figure. The blue dots illustrate the sample observed at $0.20 \leq z \leq 0.35$ evolved in both I-band and 24 μm luminosities to match the distribution at $0.35 \leq z \leq 0.5$ (shown in red dots as a comparison). The solid vertical line is the luminosity, corresponding to the I-band limiting magnitude ($I = 20$) at $z = 0.35$, below which a galaxy will be excluded from our $0.35 \leq z \leq 0.5$ sub-sample. The values indicated in the missing fraction column are the percent of the 24 μm LF potentially excluded due to the bivariate selection bias (fraction of 24 μm LF contributed by objects represented by blue dots on the left of the thick vertical line) in each $L(24\ \mu$m) bin (separated by the horizontal dotted lines). The horizontal dashed line indicates the luminosity corresponding to the 24 μm completeness limit (0.27 mJy) at $z = 0.50$, above which 24 μm sub-sample at $0.35 \leq z \leq 0.5$ is complete. We quantified the missing LF due to this effect to be less than 2% at $L(24\ \mu$m) above the completeness limit, indicating that our spectroscopic targeting method did not exclude significant numbers of MIR-bright, optically-faint galaxies.

3.4. *Bivariate Selection Bias*

Since AGES spectroscopy was targeted on a flux-limited I-band parent catalog, our sample could be affected by biases created by excluding 24 μm-bright, optically faint galaxies. This *bivariate selection bias* may result in a sample that systematically excludes galaxies with optically obscured star formation.

We quantify the possible bias by estimating the fraction of the 24 μm number densities excluded because their contributing sources fall below the I-band flux limit. This can be done by constructing a 24 μm LF as a function of I-band luminosity (*bivariate luminosity function, or BLF*) of a model sample constructed by evolving a sample at lower redshift, where it is complete to a fainter I-band luminosity, to a higher redshift bin of interest. To illustrate this experiment, consider the BLF in Figure 5. In this case, we are investigating the bivariate selection effect for $0.35 \leq z \leq 0.50$. We construct a model sample by evolving a sample from $0.20 \leq z \leq 0.35$ (which is complete to deeper luminosity) in both I-band and 24 μm to construct a BLF at $0.35 \leq z \leq 0.50$. As illustrated in Figure 5, some objects would fall below the luminosity corresponding to the I-band flux limit ($I = 20.0$) at the low-redshift edge of the bin ($z = 0.35$) and would therefore be excluded from our sample, resulting in a fraction of the missing 24 μm LF. We found, however, that this fraction is small ($< 2\%$) in this redshift bin, for 24 μm luminosities above our 24 μm completeness flux.

To model the evolution of $L(I)$, we refer to Willmer et al. (2006) and Brown et al. (2007) who found that the optical characteristic magnitudes brighten by ~ 1.3 mag per unit redshift, which would correspond to a luminosity evolution law $L \propto (1+z)^{1.6}$ at $0 \leq z \leq 1$. For the 24 μm luminosity evolution model, we adopted $L \propto (1 + z)^{3.3}$ based on Pozzi et al. (2004); Le Floc'h et al. (2005) and Pérez-González et al. (2005).

We repeated this test for the other two higher redshift bins and found that the bivariate selection bias is negligible in the $0.20 \leq z \leq 0.35$ bin; none of galaxies is excluded from the sample in this redshift bin due to bivariate selection bias. Only in the highest redshift bin, $0.50 \leq z \leq 0.65$, does the missing fraction become more significant. In this bin we found the missing fraction in the $L(24\ \mu$m) bins of $10^{10.7}$, $10^{10.9}$, and $10^{11.1}$ $L_\odot$ to be 8.7%, 4.4%, and 0.0% respectively.

The bivariate selection biases are under 5% for all but the lowest luminosity bin of our highest redshift sub-sample. We correct for it by by applying a correction factor based on the missing fraction estimated for each bin of the $1/V_{max}$ LF. This correction is included in the
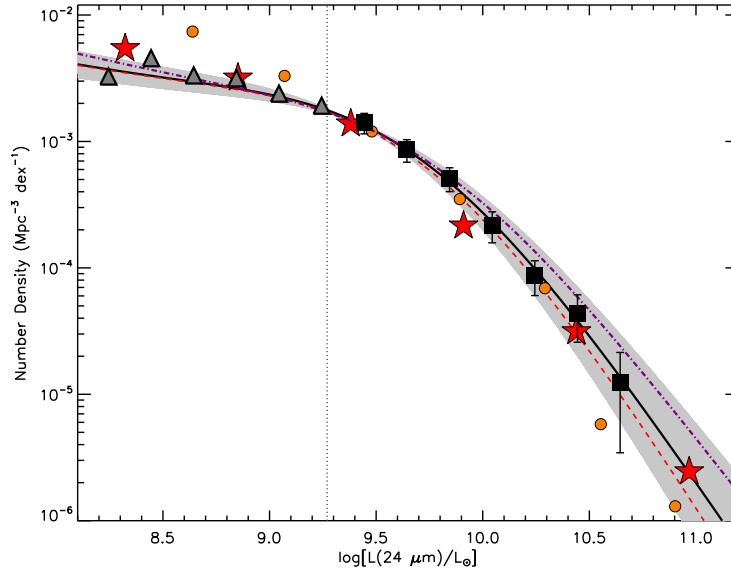
Figure 6. Mid-IR local luminosity function (LLF). We construct the LLF for the all-galaxy (solid black line) and star-forming (dashed red line) samples. The $1/V_{max}$ LLF points are shown in black squares above the luminosity corresponding to the 24 μm completeness flux limit at the upper limit of redshift range where we select the sub-sample to construct the LLF (0.27 mJy at $z = 0.25$, vertical line) and lower-limits (upward triangles) below this completeness threshold. Note that this completeness limit does not affect the maximum likelihood estimator (MLE) LLF. Uncertainties in the bright and faint-end slopes of the MLE LLF derived from the jackknife analysis are illustrated by the shaded area. The mid-IR LLFs from Rush et al. (1993); Shupe et al. (1998) and Sanders et al. (2003) are corrected for bandpass differences and shown in circles, dot-dashed line, and stars, respectively. The consistency of our LLF shape with previous work shows that it is a reliable local anchor point to study the evolution of the LF.
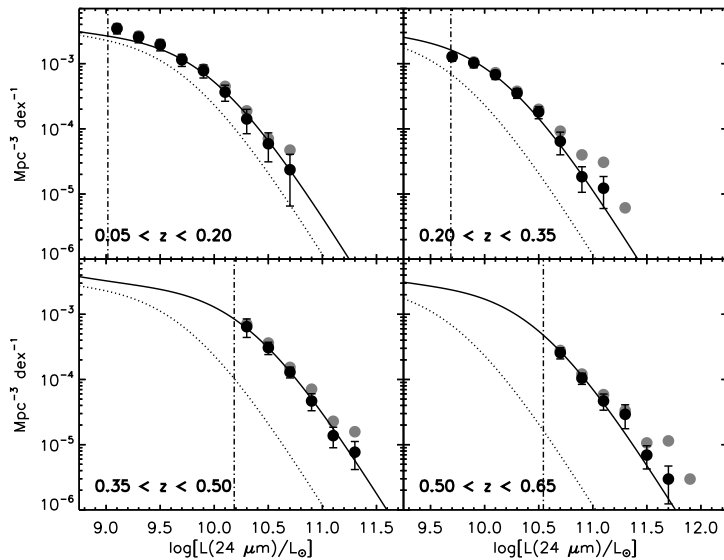

Figure 7. Evolution of the 24 μm luminosity function (LF) of star-forming galaxies (black circles) and all galaxies (gray circles, error bars omitted for clarity) for four redshift bins between $0.05 \leq z \leq 0.65$. The dotted LF is the local 24 μm LF of star-forming galaxies determined by the maximum likelihood estimator and the solid line in each panel is the local LF evolve to fit the star-forming galaxy $1/V_{max}$ LF of the corresponding redshift bin (see Sections 3.5 and 4.2). The vertical dot-dashed lines indicate the luminosity corresponding to the 24 μm completeness flux at the upper limit of the redshift bin, above which our sample is complete. We note that the $1/V_{max}$ LF in the lowest redshift bin could be affected by the overdense region near $z \simeq 0.15$ (see Figure 1). The strong evolution of the LF can be described by pure-luminosity evolution.

LF shown in Figure 7. In a broader picture, this test indicates that our spectroscopic targeting method does not systematically exclude MIR-bright, optically-faint galaxies from the final sample.

3.5. Evolution of the Luminosity Function

The evolution of the 24 μm LF is quantified using two methods. The first is to evolve the local LF template (Section 3.3) to fit the $1/V_{max}$ LF at higher redshifts so we can estimate the characteristic luminosity, L_*, and any evolution in comoving number density as a function of redshift. The second is to determine the luminosity in each redshift bin at which the cumulative number density reaches a common threshold.

In the first method, we parameterize the LF evolution assuming a functional form of

$$\psi(L, z) = g(z)\phi[L/f(z)] \qquad (3)$$

where $\phi(x)$ is given by Equation (1). The terms $f(z) = (1+z)^{\alpha_L}$, and $g(z) = (1+z)^{\alpha_D}$ describe the evolution of the luminosity and number density with redshift, respectively. We then take our LLF determined by the MLE method (Section 3.3) as a local template and fit it to the $1/V_{max}$ LF in each higher redshift bin using χ^2 minimization and the median redshift of the bin. By using the LLF as a template, we assume a fixed LF shape across the redshift range, and focus on the change in L_* and C as a function of redshift. To fit the LF template to the $1/V_{max}$ LF, we only consider $1/V_{max}$ data points above the luminosity corresponding to the 80% completeness flux threshold (0.27 mJy) at the upper redshift limit of the bin. Below this luminosity our sample in the corresponding redshift bin is no longer complete. The fit is done in two ways: fitting all redshift bins simultaneously to estimate the global evolution of the LF at $0.0 \leq z \leq 0.6$, and fitting each bin individually to explore any bin-specific deviations from the global law. We also integrate the individually fitted LFs over luminosity to determine the luminosity density, which will be used to estimate the star formation rate density ($\dot{\rho}_*$ Section 3.6).

As mentioned in Section 3.3, the LLF is affected by the evolution of IR galaxies within the redshift bin where the LLF was constructed. With a known median redshift of the LLF sample ($z = 0.17$ for both star-forming and all-galaxy samples), we can use χ^2 minimization to give the best fit evolution law that would evolve the L_* of the LLF from $L_*(z_{median})$ back to $L_*(z = 0)$ and simultaneously evolve the LLF with $L_*(z = 0)$ to fit the $1/V_{max}$ LF at all higher redshift bins. After using the global luminosity evolution constraint to evolve L_* back to $z = 0$, we can then use $L_*(z = 0)$ as a local anchor point to quantify the luminosity evolution in each bin individually.

In the second method to quantify luminosity evolution, we determined the luminosity at which the corresponding cumulative number density reaches a common arbitrary threshold in each redshift bin. The *individual* fit of the LF is integrated downward in luminosity from the bright-end until the integrated number density reaches 10^{-4}Mpc^{-3}. This method robustly quantifies the luminosity evolution because the bright-end of our LF is very well constrained and little affected by incompleteness.

3.6. Estimation of SFR

We adopt the SFR calibration of Rieke et al. (2009) to estimate the SFR from the observed $F_\nu(24\ \mu\text{m})$. Every SFR indicator using infrared luminosity is based on the assumption that UV radiation from young stars is efficiently reprocessed into IR radiation, and that the fraction of UV radiation escaping the star-forming regions without being reprocessed is small. This escape fraction depends strongly on the total-IR luminosity since more luminous IR emission implies greater UV and optical extinction. This relationship has been studied by comparing the $L(UV)$ and $L(\text{TIR})$ of galaxies (Schmitt et al. 2006; Buat et al. 2007), who found that the UV contribution to the total luminosity (the UV escape fraction) is about 20% for galaxies with $L(\text{TIR})$ equivalent to $L(24\ \mu\text{m}) \simeq 10^{8.65}\ L_\odot$ and decreases rapidly to 8% and 2.5% at $L(24\ \mu\text{m}) \simeq 10^{9.6}\ L_\odot$ and $L(24\ \mu\text{m}) \simeq 10^{10.1}\ L_\odot$, respectively. Therefore the calorimetric condition can be assumed for our normal star-forming galaxies, whose $L(24\ \mu\text{m})$ are in the range of $10^8 - 10^{10}\ L_\odot$, although the error will increase between 10^8 and $10^{8.65}\ L_\odot$. This is relevant only at the lowest redshifts. We note that the Rieke et al. (2009) 24 μm SFR calibration has a scatter of < 0.2 dex, but a relative trend such as the $\dot{\rho}_*$ evolution law will not be affected by this scatter so long as the sample is large. The luminosity density that we use to estimate the star formation rate density ($\dot{\rho}_*$) is calculated by integrating the fitted LFs (Section 3.5) in each redshift bin over luminosity from 10^6 to $10^{15}\ L_\odot$.

The IR SFR indicators are calibrated with local SEDs. Employing these indicators at higher redshifts carries an assumption of no or little SED evolution over the relevant range of z (to 1.2). This assumption is supported by Marcillac et al. (2006), Bavouzet et al. (2008) and Magnelli et al. (2009). There are indications that, at redshifts of $z \sim 2$, the calibration of the observed 24 μm flux density and SFR may shift from values deduced from local SED templates (Papovich et al. 2007; Rigby et al. 2008; Farrah et al. 2008). The primary cause of these changes appears to be that the aromatic bands tend to be stronger for a given luminosity at high redshift, so the SEDs resemble more closely those of local galaxies with significantly smaller total infrared luminosity. The probable cause of this behavior is that local ULIRGs tend to have intense star formation concentrated into very optically thick nuclear regions, whereas galaxies of similar infrared luminosity at high redshift probably have more widely distributed star forming regions of lower optical depth. It is unlikely that this effect significantly alters the calibration of SFRs in this paper. First, the effect appears to be weaker for normal star-forming galaxies and galaxies of LIRG-level luminosity even at high redshift (Rigby et al. 2008); the galaxies that dominate our study are of lower luminosity still. Second, given their relatively low redshifts, the observed 24 μm flux densities from our galaxies are not strongly affected by the aromatic band strengths. Third, the evolutionary state of our galaxies should resemble local galaxies at least as much as it does those at $z \sim 2$; in fact, Magnelli et al. (2009) show that the SEDs of infrared galaxies for $0.4 \leq z \leq 1.2$ resemble those of local galaxies reasonably closely.

3.7. Uncertainties Analysis for the LF and SFR

We use jackknife resampling to estimate the uncertainties in our $1/V_{max}$ LFs and the LLF parameters (α, β, L_*, and the normalization factor; see Section 3.3), as well as star formation rate density and evolution laws derived from the LFs.

The AGES survey used 15 overlapping tiles corresponding to the Hectospec field of view. These tiles are a natural way to build 15 jackknife samples, each dropping one of these roughly 1-degree diameter tiles and then using the variance in parameter estimates for these 15 subsamples to estimate the uncertainties. This procedure will include Poisson uncertainties and sub-degree-scale cosmic variance effects. It will underestimate uncertainties due to larger scale correlations between galaxies.

We can estimate the large scale effects by shifting the entire LF estimation for each redshift bin by our estimate of the total cosmic variance and recalculating the parameters. The cosmic variance on the scale of our survey volume ($\sim 10^6 \mathrm{Mpc}^3$) can be estimated using Peebles (1980) and by assuming the power-law correlation function estimated from the SDSS for late-type galaxies, $\xi = (r/r_0)^{-\gamma}$, with $r_0 = 3.6\ h^{-1}\mathrm{Mpc}$ and $\gamma = 1.7$ (Zehavi et al. 2005). In the bins of redshift $0.05 \leq z \leq 0.20, 0.20 \leq z \leq 0.35, 0.35 \leq z \leq 0.50$, and $0.50 \leq z \leq 0.65$, we expect the uncertainties on the LF due to cosmic variances to be 15%, 11%, 10%, and 9%, respectively (Dai et al. 2009).

4. RESULTS

Here we will discuss our determination of the local 24 μm LF and compare it to other studies (Section 4.1) to establish a baseline for our study of LF evolution to $z \sim 0.6$ (Section 4.2). Next, we discuss the evolution constraints based on the combination of our Boötes field data and the 35 μm LF evolution from Magnelli et al. (2009) who focused on $0.4 \leq z \leq 1.3$ (Section 4.3) using the FIDEL survey. The combination of these two studies lets us determine the $\dot{\rho}_*$ evolution from $0 \leq z \leq 1.2$ in a unified and accurate way. We will then present the local star formation rate density and the star formation rate density evolution derived from the LFs (Section 4.4).

4.1. Local 24 μm Luminosity Functions

The local 24 μm LFs for both the star-forming and all-galaxy populations are shown in Figure 6. Both LLFs are constructed from a sample at $0.05 \leq z \leq 0.25$ (median redshift $z = 0.17$) and evolved back to $z = 0.0$ using the global evolution law estimated in Section 3.5. Their shape parameters are tabulated in Table 1 along with other estimates of the LLF using the double-power law form of equation.

The star-forming and all-galaxy LLFs have identical faint-end slopes, but the star-forming LLF has a slightly steeper bright-end slope and a brighter characteristic luminosity. Both differences are within the uncertainties of the respective parameters, but nevertheless the steeper slope of the star-forming LLF is expected because the sample excluded the IR-luminous AGN, as illustrated in Figure 4. This comparison shows that the overall impact of AGN on the LLF is small, and that any residual unidentified AGN should have little effect on our conclusions. In Figure 6 we present our LLF along with the

Table 2
The 24 μm and Total-IR Luminosities Above Which the Cumulative Number Density of Star-Forming Galaxies is $10^{-4}\mathrm{Mpc}^{-3}$ for Each Redshift Bin

Redshift Bin	$L(24\ \mu\mathrm{m})$ $10^{10}L_\odot$	$L(\mathrm{TIR})$[a] $10^{10}L_\odot$
$0.05 \leq z \leq 0.20$	1.2 ± 0.4	9.2 ± 2.9
$0.20 \leq z \leq 0.35$	1.7 ± 0.4	13.2 ± 3.0
$0.35 \leq z \leq 0.50$	2.5 ± 0.5	18.9 ± 3.7
$0.50 \leq z \leq 0.65$	3.9 ± 0.7	28.1 ± 5.3

[a] $L(\mathrm{TIR})$ is estimated using the Rieke et al. (2009) formalism.

bandpass and cosmologically adjusted $1/V_{max}$ LLF of Rush et al. (1993), Sanders et al. (2003) and Pozzi et al. (2004), and the MLE LLF of Shupe et al. (1998).

One of the most important parameters of the LLF is the value of $L_*(z = 0)$. Our L_* estimates for the star-forming and all-galaxy populations are $(4.27 \pm 0.71) \times 10^9$ and $(4.07 \pm 0.67) \times 10^9\ L_\odot$, respectively. We compare our results with other works that adopt the double power-law form of LF by correcting for cosmological assumptions and bandpasses using the Rieke et al. (2009) SED library. The Shupe et al. (1998) LLF using IRAS 25 μm measurements reports a local L_* of $(4.67 \pm 0.41) \times 10^9$ $L_\odot$, which corresponds to $(4.47 \pm 0.40) \times 10^9\ L_\odot$ when corrected for the difference between the IRAS 25 μm and MIPS 24 μm bandpasses. Xu et al. (1998) report an ISO 15 μm local L_* of $(4.79 \pm 1.69) \times 10^9\ L_\odot$, corresponding to $(6.40 \pm 2.25) \times 10^9\ L_\odot$ at 24 μm. Sanders et al. (2003) report a local total-IR L_* of $10^{10.5}L_\odot$, which corresponds to a 24 μm L_* of $4.4 \times 10^9\ L_\odot$. Our estimate of L_* agrees well with all these other studies. More importantly, the extrapolation of the LLF L_* back to $z = 0.0$ using the luminosity evolution constraint from our full sample ensures that these values reflect an accurate value at $z = 0$ in addition to providing the best-match LLF template to study the evolution of the LF in our sample.

4.2. Evolution of the 24 μm LF

Strong luminosity evolution is evident in the $1/V_{max}$ LFs over the redshift range $0.05 \leq z \leq 0.65$ shown in Figure 7. We considered two evolutionary scenarios for the 24 μm LF parameterized by Equation (3), including pure luminosity evolution and pure density evolution. These scenarios were tested by evolving our local 24 μm LF to fit the $1/V_{max}$ LF at higher redshift by χ^2 minimization. We cannot constrain a combined luminosity and density evolution model because we do not sample below L_* in these higher redshifts sub-samples. The density evolution model can be rejected on the basis of the χ^2 values with high confidence. Other studies have found that the density evolution is small. Le Floc'h et al. (2005) and Pérez-González et al. (2005) derived a density evolution laws of $\phi^* \propto (1+z)^{0.7^{+0.2}_{-0.6}}$ and $\phi^* \propto (1+z)^{1.0 \pm 0.3}$, respectively. More recently, Magnelli et al. (2009) used a stacking analysis to study the evolution of the 35 μm LF and reported density evolution given by $\phi^* \propto (1+z)^{0.1 \pm 0.7}$ at $z \lesssim 1.2$. This implies a density variation of about $5\% \pm 40\%$ at $0.0 \leq z \leq 0.6$, which is comparable to the uncertainties due to cosmic variance in the density.
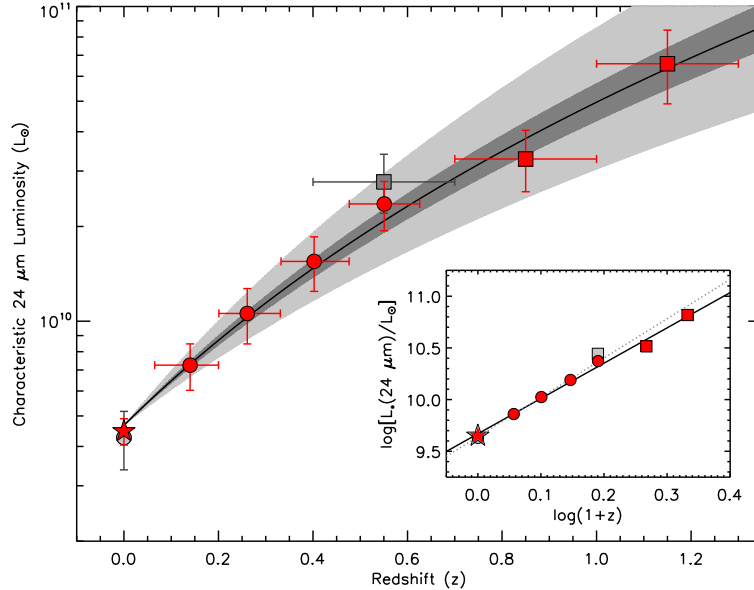
Figure 8. Evolution of the characteristic 24 μm luminosity of galaxies, L_*, to $z \sim 1.2$ based on our results (red circles) and that of Magnelli et al. (2009) using FIDEL (red squares). The light shaded area is the luminosity evolution law $L_* \propto (1+z)^{\alpha_L}$ bounded by α_L of 2.7 and 4.2 from the lowest and highest uncertainty limits of Pérez-González et al. (2005) and Magnelli et al. (2009), respectively. The combined evolution law, $L_{*,combined} \propto (1+z)^{3.4\pm0.2}$, is shown as a solid line with the uncertainties from the combined fit shown by the dark shaded area. The local point for the global fit (red star) is that of Shupe et al. (1998) converted to 24 μm. Two data points were excluded from the fit (see details in Section 4.3) and are shown in gray. Inset: the combined of luminosity evolution (solid line) with the same symbols as the main figure (error bars are omitted for clarity) and the fit (dotted line) based on the Boötes data alone, $(1+z)^{3.8\pm0.3}$.
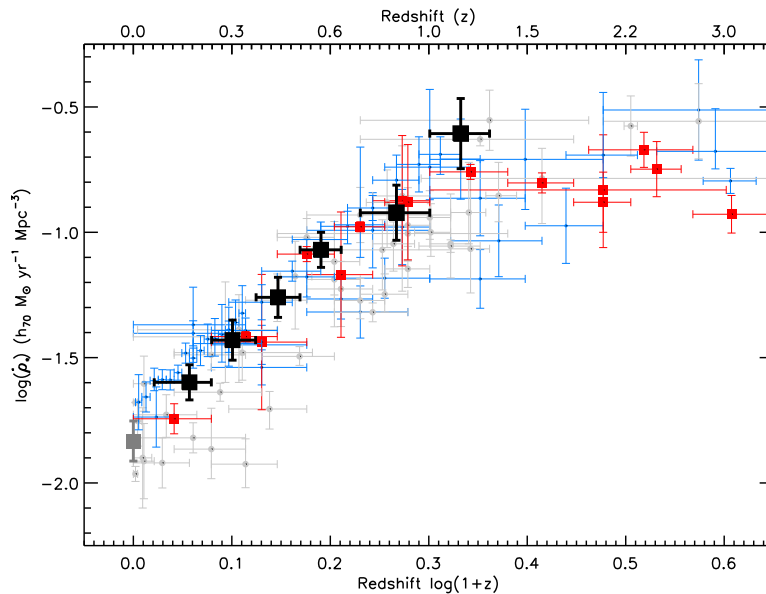

Figure 9. Evolution of the star formation rate density ($\dot{\rho}_*$) as a function of redshift assuming Salpeter (1955) IMF. Our $\dot{\rho}_*$ estimates are shown in large black squares and our extrapolated local point (Section 4.1) shown in gray, compared to the $\dot{\rho}_*$ from the following. The extinction-corrected UV $\dot{\rho}_*$ from the compilation of Hopkins (2004) and Hopkins & Beacom (2006) are shown in blue circles; IR $\dot{\rho}_*$ in red squares (Hopkins 2004; Pérez-González et al. 2005; Reddy et al. 2008); gray dots are the radio (1.4 GHz), X-ray, and extinction-corrected [OII], Hα, and Hβ $\dot{\rho}_*$ (Hopkins 2004; Seymour et al. 2008; Smolčić et al. 2009; Zhu et al. 2009). The agreement of our $\dot{\rho}_*$ normalization and those from extinction-corrected optical and UV observations confirms that a majority of star formation at $z < 1.2$ is obscured and can be directly traced by 24 μm observation.

Table 3
Evolution of the Characteristic 24 μm Luminosity,
L$_*$(24 μm), and the Star Formation Rate Density, $\dot{\rho}_*$,
to $z \sim 1.2$

Redshift	L$_*$(24 μm) 10^9 $L_\odot$	log($\dot{\rho}_*$)[a]
0.00 (this work)	4.27 ± 0.71	−1.83± 0.08
0.00 (Shupe et al. 1998)	4.47 ± 0.40	−1.71± 0.04
$0.05 \leq z \leq 0.20$	7.25 ± 1.12	−1.60± 0.07
$0.20 \leq z \leq 0.35$	10.6 ± 1.8	−1.43± 0.08
$0.35 \leq z \leq 0.50$	15.5 ± 2.4	−1.26± 0.08
$0.50 \leq z \leq 0.65$	23.6 ± 3.6	−1.07± 0.07
$0.7 \leq z \leq 1.0$[b]	32.8 ± 7.8	−0.92± 0.11
$1.0 \leq z \leq 1.3$[b]	65.8 ± 18.8	−0.61± 0.14

[a] $\dot{\rho}_*$ estimates assume a Salpeter (1955) IMF and are given in the unit of $M_\odot \text{yr}^{-1} \text{Mpc}^{-3}$. Assuming the Kroupa (2002) IMF would yield 0.66 $\dot{\rho}_*$ given here.
[b] Based on FIDEL luminosity functions (Magnelli et al. 2009).

Using a pure luminosity evolution model, we obtain an evolution law given by $L_*(24~\mu\text{m}) \propto (1+z)^{3.8\pm0.3}$ for the star-forming sample. This luminosity evolution is shown as a fit to the $1/V_{\max}$ LF in Figure 7. One of the evolution descriptions of Pérez-González et al. (2005) uses pure luminosity evolution with the Schechter (1976) form of LF. They report luminosity evolution of $(1+z)^{3.6\pm0.3}$ for $z < 0.8$, agreeing with our result. The evolution of the LF was also quantified by determining the luminosity above which the cumulative number density reached 10^{-4}Mpc^{-3}; as tabulated in Table 2. This luminosity increases by more than a factor of three from a redshift of 0.05 to 0.65. We should note that while we cannot jointly constrain luminosity and density evolution, the simple power-law model is an adequate description of our data. Improving on it would require a deeper sample in a comparably large area to the Boötes field.

Our method to determine evolution of the LF assumes no evolution in LF shape from the local template. The template, however, yields a better fit at low redshift than in the higher redshift bins. Discrepancies between the template and the data are most visible at $0.50 \leq z \leq 0.65$ (Figure 7). This discrepancy could be due to an intrinsic evolution toward a shallower bright-end slope at higher redshifts. On the other hand, it could indicate a contribution from unidentified AGN in the higher 24 μm luminosity regime. The latter explanation is consistent with the observation that AGN are progressively more abundant at higher redshifts (Figure 4) as well as from Figure 7 itself, which shows that the bright-end slope of the $1/V_{\max}$ LF of all galaxies (including AGN) becomes shallower to a greater extent compared to that of the star-forming galaxy LF.

4.3. Extending the LF evolution constraint to $z \sim 1.2$

We augment our LF evolution constraint at low and intermediate redshifts with the result of Magnelli et al. (2009) at 35 μm. This is a useful combination because Magnelli et al. (2009) used the deep (50 μJy and 3 mJy at 24 and 70 μm, respectively), narrow-field (0.5 sq. deg.), FIDEL survey. The FIDEL sample has ~ 7000 and ~ 600 star-forming galaxies detected at 24 μm and 70 μm, respectively, with known redshifts. AGN were excluded on the basis of deep (200 ks - 2 Ms) X-ray ob-

servations. Additionally, Magnelli et al. (2009) employ a stacking analysis to provide further constraints for the LFs. Their approach provides one of the best evolution constraints for the LFs at higher redshifts to date but will be affected by cosmic variance at intermediate redshifts, where our results should be more reliable. In addition, the rest frame 35 μm values can be corrected to 24 μm with minimal uncertainties due to luminosity conversions.

We need to correct Magnelli et al. (2009) for (1) bandpass differences; and (2) k-correction differences (SED assumptions). To correct for bandpass differences, we use the Rieke et al. (2009) SED library to calculate a luminosity-dependent conversion factor between the Magnelli et al. (2009) rest-frame 35 μm, which was observed at 70 μm and k-corrected to $z = 1$ (the observed 70 μm band probes the 35 μm rest-frame SED at $z = 1$). This conversion factor varies slowly from 0.5 at $L(\text{TIR}) \sim 10^{10} L_\odot$ to 0.3 at $L(\text{TIR}) \sim 10^{12} L_\odot$. Next we compare the consistency of the Chary & Elbaz (2001) SED used by Magnelli et al. (2009) and our Rieke et al. (2009) SED. The best test for differences lies in the $L_*(z = 0)$ anchor point, $L_*(z = 0, 35~\mu\text{m}) = 10^{9.85} L_\odot$, that Magnelli et al. (2009) obtained by converting the Shupe et al. (1998) IRAS 25 μm L_* to 35 μm (MIPS 70 μm observed bandpass at $z = 1$) using the Chary & Elbaz (2001) SED. Converting this $L_*(z = 0, 35~\mu\text{m})$ back to our MIPS 24 μm rest-frame (which is about 5% fainter than the original value at 25 μm) using the Rieke et al. (2009) SED would yield $L_*(z = 0, 24~\mu\text{m})$ of $3.72 \times 10^9~h^{-2} L_\odot$, which is 20% lower than the original Shupe et al. (1998) value tabulated in Table 1. In other words, a 20% discrepancy resulted from subjecting a luminosity through this conversion exercise and we must apply a +20% correction factor to the FIDEL data points to correct for SED differences.

For the combined fit, we omitted two data points. First, we dropped the lowest redshift Magnelli et al. (2009) bin ($0.4 \leq z \leq 0.7$), which overlaps with our highest redshift bin, because this redshift bin will be more strongly affected by cosmic variance since our highest redshift bin encompasses about an order of magnitude more volume. Second, we dropped our local point because it was estimated by evolving the sample in the lowest redshift bin ($0.05 \leq z \leq 0.20$) back to $z = 0.0$ based on the higher redshift bins (Section 3.5), so including this point would "double count" the data. Instead we use the Shupe et al. (1998) local point converted to 24 μm. Note, however, that our local L_* estimate is consistent with Shupe et al. (1998). The combined fit (shown in Figure 8) yields a slightly shallower evolution law than that estimated from the Boötes field alone (Section 4.2), with $L_{*,combined} \propto (1+z)^{3.4\pm0.2}$.

4.4. The Evolution of the Star Formation Rate Density

Now that we have constructed the LF and determined the luminosity evolution from $z = 0.0$ to 1.2 we can provide a complete picture of the $\dot{\rho}_*$ evolution from $z = 0.0$ to $z \sim 1.2$. We compute SFRs based on Kroupa (2002) IMF used by Rieke et al. (2009). This leads to estimates of $\dot{\rho}_*$ a factor of 0.66 lower than those assuming a Salpeter (1955) IMF with a single power-law slope of -1.35 from 0.1 to 100 $M_\odot$.

Our estimates for $\dot{\rho}_*$ in each redshift bin to $z \sim 1.2$, including both our results and the adjusted values from Magnelli et al. (2009), are tabulated in Table 3, and shown in Figure 9 along with $\dot{\rho}_*$ measurements from other wavelengths from the UV to radio. Based on the fit of the combined data out to $z \sim 1.2$, our $\dot{\rho}_*$ evolution law is given by

$$\log(\dot{\rho}_*) = (3.5 \pm 0.2)\log(1+z) - 1.96 \pm 0.08 \quad (4)$$

At $z = 0$ our fit yields a local $\dot{\rho}_*$ of $(1.09 \pm 0.21) \times 10^{-2} M_\odot \mathrm{yr}^{-1} \mathrm{Mpc}^{-3}$ for Kroupa (2002), which corresponds to $\dot{\rho}_*$ of $(1.65 \pm 0.32) \times 10^{-2} M_\odot \mathrm{yr}^{-1} \mathrm{Mpc}^{-3}$ for a Salpeter (1955) IMF. Our estimate agrees with previous works on the local $\dot{\rho}_*$ that have properly accounted for the internal extinction of the galaxy. Without such corrections the $\dot{\rho}_*$ will be underestimated by $50 - 70$ % (Gallego et al. 1995; Tresse & Maddox 1998; Hanish et al. 2006; Salim et al. 2007). The agreement between $\dot{\rho}_*$ estimates corrected for internal extinction and our $\dot{\rho}_*$ derived from 24 μm luminosity suggests that $\sim$half of the local star formation is obscured and the MIR provides a direct and reliable means for SFR measurement.

Figure 9 illustrates the good agreement of the normalization of our $\dot{\rho}_*$ estimates and those derived from the UV observation corrected for the effects of intrinsic extinction of the target galaxies (normalization corrections can be as large as 0.7-dex; e.g., Figure 5 of Schiminovich et al. (2005) illustrates the extent of the required correction for the UV observations). Hopkins (2004) reports the fit to a compilation of the $\dot{\rho}_*$ that has been corrected for extinction of the target galaxies with an assumption of a luminosity-dependent obscuration. The resulting best fit is given by $\log(\dot{\rho}_*) = (3.29 \pm 0.26)\log(1+z) - 1.98 \pm 0.04$ (assuming the Kroupa (2002) IMF), which also agrees well with our evolution determined from the combination of the NDWFS and the FIDEL results. Again, this agreement confirms that star formation at redshift $0.0 < z < 1.2$ occurs in obscured environments and can be traced directly with 24 μm observations given a proper classification and exclusion of AGNs. It should be noted that our result is consistent with findings of Takeuchi et al. (2005), which show an evolution of the fraction of obscured star formation from 50% locally to $> 80\%$ at $z \sim 1$.

5. CONCLUSIONS

We study the evolution of 24 μm-selected galaxies by constructing their 24 μm (rest-frame) luminosity functions (LF). Our sample contains 4,047 galaxies with spectroscopic redshifts at $0.0 \leq z \leq 0.65$ in the Boötes field of the NOAO Deep-Wide Field Survey (NDWFS). The 24 μm data and spectroscopic redshifts were obtained with *Spitzer* and with the AGN and Galaxies Evolution Survey (AGES), respectively. Our sample is a unique combination of wide field, spectroscopic redshifts, and 24 μm imaging that is ideal for intermediate redshifts where MIR galaxy evolution has not been well-studied. The large area (9 sq. deg.) of the Boötes field helps mitigate cosmic variance, which otherwise can be a serious issue at low and intermediate redshifts. Theoretically, the cosmic variance in our study is less than 10% at $z > 0.2$. Spectroscopic redshifts reduce cross-talk between redshift bins and faint/bright end slope biases and

provide an accurate number density contribution for each object.

Galaxies exhibiting AGN activities characterized by X-ray emission and mid-IR power-law are excluded from our star-forming sample. We find that the optical line diagnostics (the BPT method) are not suitable for identifying AGN dominant at mid-IR wavelengths because the mid-IR emission from optically-selected AGNs is often dominated by star formation. We identified 288 objects with 24 μm emission likely to be dominated by AGN. Excluding them leaves a sample of 3,759 star-forming galaxies.

We derive the 24 μm luminosity using calibrations derived from the most recent SED library of the mid-IR spectra from *Spitzer* (Rieke et al. 2009). Our sample is comprised mainly of normal star-forming galaxies (66% have $L(\mathrm{TIR}) < 10^{11}$ $L_\odot$) and LIRGs (33% have 10^{11} $L_\odot < L(\mathrm{TIR}) < 10^{12}$ $L_\odot$). Only 1% are ULIRGs ($L(\mathrm{TIR}) > 10^{12}$ $L_\odot$) and we found that most of the ULIRGs contain AGN.

We construct the local 24 μm luminosity function (LLF) as a template to study evolution of the LF. Our LLF was constructed at $0.05 \leq z \leq 0.25$ and evolved back to $z = 0$ simultaneously with the fit to constrain the global evolution of our sample. The LLF template for our star-forming sample is given by a double power-law with faint-end slope, $\alpha = 0.37 \pm 0.04$, bright-end slope, $\beta = 2.36 \pm 0.41$, characteristic luminosity, $L_*(z = 0) = (4.27 \pm 0.71) \times 10^9 L_\odot$, and density normalization, $C = (1.2 \pm 0.8) \times 10^{-3} \mathrm{Mpc}^{-3}$. Our major results are as follows.

1. The evolution of the LF at $z \leq 0.65$ can be represented by pure luminosity evolution with the characteristic 24 μm luminosity of star-forming galaxies evolving as $L_*(24 \mu m) \propto (1+z)^{3.8 \pm 0.3}$. We demonstrate by the construction of the bivariate I-band and 24 μm luminosity function that the fraction of missing 24 μm-luminous, optically-faint galaxies due to our I-band magnitude limit for spectroscopic targeting is very small.

2. We extend the constraint on the evolution of L_* to $z \sim 1.2$ by combining our results with the higher redshift results from Magnelli et al. (2009) based on the FIDEL survey. The combined sample gives a slightly shallower luminosity evolution of $L_*(24 \mu m) \propto (1+z)^{3.4 \pm 0.2}$. The shallower evolution law derived by including the FIDEL sample at redshifts of $z = 0.85$ and 1.15 suggests that the evolution in $\dot{\rho}_*$ may begin to slow compared to lower redshifts.

3. The local star formation rate density based on our 24 μm data is $\dot{\rho}_*$ of $(1.09 \pm 0.21) \times 10^{-2} M_\odot \mathrm{yr}^{-1} \mathrm{Mpc}^{-3}$ assuming the Kroupa (2002) IMF, which corresponds to $\dot{\rho}_*$ of $(1.65 \pm 0.32) \times 10^{-2} M_\odot \mathrm{yr}^{-1} \mathrm{Mpc}^{-3}$ for a Salpeter (1955) IMF. The combined evolution constraint for the LF at $z \leq 1.2$ indicates that $\dot{\rho}_*$ evolves as $\dot{\rho}_* \propto (1+z)^{3.5 \pm 0.2}$. Our normalization and evolution measurements agree well with the $z \lesssim 1$ extinction-corrected findings from other studies, which confirms that most of star formation is obscured and that 24 μm serves as a direct and reliable $\dot{\rho}_*$ indicator in these cases.

REFERENCES

Alonso-Herrero, A., Rieke, G. H., Rieke, M. J., Colina, L., Pérez-González, P. G., & Ryder, S. D. 2006, ApJ, 650, 835
Ashby, M. L. N., et al. 2009, ApJ, 701, 428
Baldwin, J. A., Phillips, M. M., & Terlevich, R. 1981, PASP, 93, 5
Barmby, P., et al. 2006, ApJ, 642, 126
Bavouzet, N., Dole, H., Le Floc'h, E., Caputi, K. I., Lagache, G., & Kochanek, C. S. 2008, A&A, 479, 83
Bertin, E., & Arnouts, S. 1996, A&AS, 117, 393
Blanton, M. R., & Roweis, S. 2007, AJ, 133, 734
Brand, K., et al. 2006, ApJ, 641, 140
Brand, K., et al. 2009, ApJ, 693, 340
Brown, M. J. I., Dey, A., Jannuzi, B. T., Brand, K., Benson, A. J., Brodwin, M., Croton, D. J., & Eisenhardt, P. R. 2007, ApJ, 654, 858
Buat, V., Donas, J., Milliard, B., & Xu, C. 1999, A&A, 352, 371
Buat, V., et al. 2007, ApJS, 173, 404
Cardamone, C. N., et al. 2008, ApJ, 680, 130
Caputi, K. I., et al. 2007, ApJ, 660, 97
Chary, R., & Elbaz, D. 2001, ApJ, 556, 562
Chary, R.-R. 2007, Deepest Astronomical Surveys, 380, 375
Dai, X., et al. 2009, ApJ, 697, 506
Dale, D. A., Helou, G., Contursi, A., Silbermann, N. A., & Kolhatkar, S. 2001, ApJ, 549, 215
Dale, D. A. & Helou, G. 2002, ApJ, 576, 159
Dale, D. A., et al. 2007, ApJ, 655, 863
Donley, J. L., Rieke, G. H., Pérez-González, P. G., Rigby, J. R., & Alonso-Herrero, A. 2007, ApJ, 660, 167
Donley, J. L., Rieke, G. H., Pérez-González, P. G., & Barro, G. 2008, ApJ, 687, 111
Dole, H., et al. 2004, ApJS, 154, 87
Eisenhardt, P. R., et al. 2004, ApJS, 154, 48
Elbaz, D., et al. 1999, A&A, 351, L37
Elbaz, D., et al. 2007, A&A, 468, 33
Elvis, M., et al. 1994, ApJS, 95, 1
Fabricant, D. et al. 2005, PASP, 117, 1411
Farrah, D., et al. 2008, ApJ, 677, 957
Franceschini, A., Aussel, H., Cesarsky, C. J., Elbaz, D., & Fadda, D. 2001, A&A, 378, 1
Gallego, J., Zamorano, J., Aragon-Salamanca, A., & Rego, M. 1995, ApJ, 455, L1
Gordon, K., et al. 2005, PASP, 117, 503
Gorjian, V., et al. 2008, ApJ, 679, 1040
Hacking, P., & Houck, J. R. 1987, ApJS, 63, 311
Hacking, P., Houck, J. R., & Condon, J. J. 1987, ApJ, 316, L15
Hanish, D. J., et al. 2006, ApJ, 649, 150
Hickox, R. C., et al. 2009, ApJ, 696, 891
Hopkins, A. M. 2004, ApJ, 615, 209
Hopkins, A. M., & Beacom, J. F. 2006, ApJ, 651, 142
Houck, J. R., et al. 2005, ApJ, 622, L105
Huchra, J. & Sargent, W. L. W. 1973, ApJ, 186, 433
Ivezić, Ž., et al. 2002, AJ, 124, 2364
Jannuzi, B. T., & Dey, A. 1999, Photometric Redshifts and the Detection of High Redshift Galaxies, 191, 111
Kauffmann, G., et al. 2003, MNRAS, 346, 1055
Kennicutt, R. C. 1998, ARA&A, 36, 189
Kewley, L. J., Dopita, M. A., Sutherland, R. S., Heisler, C. A., & Trevena, J. 2001, ApJ, 556, 121
Kewley, L. J., Groves, B., Kauffmann, G., & Heckman, T. 2006, MNRAS, 372, 961
Kroupa, P. 2002, Science, 295, 82
Lacy, M., et al. 2004, ApJS, 154, 166
Lagache, G., Dole, H., & Puget, J.-L. 2003, MNRAS, 338, 555
Lagache, G., et al. 2004, ApJS, 154, 112
Le Floc'h, E., et al. 2005, ApJ, 632, 169
LeFloc'h, E., et al. 2009, ApJ, 703, 222

Leitherer, C., et al. 1999, ApJS, 123, 3
Lilly, S. J., Le Fevre, O., Hammer, F., & Crampton, D. 1996, ApJ, 460, L1
Lilly, S. J., et al. 2007, ApJS, 172, 70
Madau, P., Ferguson, H. C., Dickinson, M. E., Giavalisco, M., Steidel, C. C., & Fruchter, A. 1996, MNRAS, 283, 1388
Magnelli, B., Elbaz, D., Chary, R. R., Dickinson, M., Le Borgne, D., Frayer, D. T., & Willmer, C. N. A. 2009, A&A, 496, 57
Marcillac, D., Elbaz, D., Chary, R. R., Dickinson, M., Galliano, F., & Morrison, G. 2006, A&A, 451, 57
Martin, C., et al. 2003, Proc. SPIE, 4854, 336
Marleau, F. R., et al. 2004, ApJS, 154, 66
Marleau, F. R., Fadda, D., Appleton, P. N., Noriega-Crespo, A., Im, M., & Clancy, D. 2007, ApJ, 663, 218
Marshall, H. L., Tananbaum, H., Avni, Y., & Zamorani, G. 1983, ApJ, 269, 35
Murray, S. S., et al. 2005, ApJS, 161, 1
Neugebauer, G., Oke, J. B., Becklin, E. E., & Matthews, K. 1979, ApJ, 230, 79
Papovich, C., et al. 2004, ApJS, 154, 70
Papovich, C., et al. 2006, AJ, 132, 231
Papovich, C., et al. 2007, ApJ, 668, 45
Peebles, P. 1980, The Large-Scale Structure of the Universe (Princeton University Press)
Pérez-González, P. G., et al. 2005, ApJ, 630, 82
Pozzi, F., et al. 2004, ApJ, 609, 122
Reddy, N. A., Steidel, C. C., Pettini, M., Adelberger, K. L., Shapley, A. E., Erb, D. K., & Dickinson, M. 2008, ApJS, 175, 48
Rieke, G. H., et al. 2004, ApJS, 154, 25
Rieke, G. H., Alonso-Herrero, A., Weiner, B. J., Pérez-González, P. G., Blaylock, M., Donley, J. L., & Marcillac, D. 2009, ApJ, 692, 556
Rieke, G. H., & Lebofsky, M. J. 1981, ApJ, 250, 87
Rieke, G. H., & Lebofsky, M. J. 1986, ApJ, 304, 326
Rigby, J. R., et al. 2008, ApJ, 675, 262
Rowan-Robinson, M., et al. 1997, MNRAS, 289, 490
Rush, B., Malkan, M. A., & Spinoglio, L. 1993, ApJS, 89, 1
Sandage, A., Tammann, G. A., & Yahil, A. 1979, ApJ, 232, 352
Sanders, D. B., Mazzarella, J. M., Kim, D.-C., Surace, J. A., & Soifer, B. T. 2003, AJ, 126, 1607
Salim, S., et al. 2007, ApJS, 173, 267
Salpeter, E. E. 1955, ApJ, 121, 161
Saunders, W., Rowan-Robinson, M., Lawrence, A., Efstathiou, G., Kaiser, N., Ellis, R. S., & Frenk, C. S. 1990, MNRAS, 242, 318
Schechter, P. 1976, ApJ, 203, 297
Schiminovich, D., et al. 2005, ApJ, 619, L47
Scoville, N., et al. 2007, ApJS, 172, 1
Schlegel, D. J., Finkbeiner, D. P., & Davis, M. 1998, ApJ, 500, 525
Schmidt, M. 1968, ApJ, 151, 393
Schmitt, H. R., Calzetti, D., Armus, L., Giavalisco, M., Heckman, T. M., Kennicutt, R. C., Jr., Leitherer, C., & Meurer, G. R. 2006, ApJ, 643, 173
Seymour, N., et al. 2008, ApJ, 681, L1
Shi, Y., et al. 2007, ApJ, 669, 841
Shupe, D. L., Fang, F., Hacking, P. B., & Huchra, J. P. 1998, ApJ, 501, 597
Smith, J. D. T., et al. 2007, ApJ, 656, 770
Smolčić, V., et al. 2009, ApJ, 690, 610
Soifer, B. T., Boehmer, L., Neugebauer, G., & Sanders, D. B. 1989, AJ, 98, 766
Soifer, B. T., & Neugebauer, G. 1991, AJ, 101, 354
Stern, D., et al. 2005, ApJ, 631, 163
Stetson, P. B. 1987, PASP, 99, 191
Takeuchi, T. T., Buat, V., & Burgarella, D. 2005, A&A, 440, L17
Tresse, L., & Maddox, S. J. 1998, ApJ, 495, 691
Willmer, C. N. A., et al. 2006, ApJ, 647, 853
Xu, C., Hacking, P. B., Fang, F., et al. 1998, ApJ, 508, 576
Xu, C. 2000, ApJ, 541, 134
Yahil, A., Strauss, M. A., Davis, M., & Huchra, J. P. 1991, ApJ, 372, 380
Zehavi, I., et al. 2005, ApJ, 630, 1
Zhu, G., Moustakas, J., & Blanton, M. R. 2009, ApJ, 701, 86